ADVANCED ENERGY MATERIALS
www.advenergymat.de

Interface Optimization via Fullerene Blends Enables Open-Circuit Voltages of 1.35 V in $CH_3NH_3Pb(I_{0.8}Br_{0.2})_3$ Solar Cells

Zhifa Liu, Johanna Siekmann, Benjamin Klingebiel, Uwe Rau, and Thomas Kirchartz**

Nonradiative recombination processes are the biggest hindrance to approaching the radiative limit of the open-circuit voltage for wide bandgap perovskite solar cells. In addition to high bulk quality, good interfaces and good energy level alignment for majority carriers at charge transport layer-absorber interfaces are crucial to minimize nonradiative recombination pathways. By tuning the lowest-unoccupied molecular-orbital of electron transport layers via the use of different fullerenes and fullerene blends, open-circuit voltages exceeding 1.35 V in $CH_3NH_3Pb(I_{0.8}Br_{0.2})_3$ device are demonstrated. Further optimization of mobility in binary fullerenes electron transport layers can boost the power conversion efficiency as high as 18.9%. It is noted in particular that the V_{oc} fill factor product is >1.096 V, which is the highest value reported for halide perovskites with this bandgap.

1. Introduction

One of the main reasons why halide perovskite solar cells have attracted so much interest over the past years is their ability to generate high open-circuit voltages relative to their respective bandgaps.[1,2] Using simple solution-based processing, open-circuit voltages within ≈ 60 mV of the radiative limit have been experimentally realized in solar cells with efficiencies exceeding 20%.[3–7] Approaching the radiative limit that closely requires nonradiative recombination processes to be very slow compared to most other semiconductors. This requirement of slow recombination must be valid in the bulk of the material[8] but also at grain boundaries and at interfaces to charge-transport layers. The fact that recombination can be extremely slow even when charge-transport layers are attached to the absorber layer[4,9–12] is most remarkable and allows combining high open-circuit voltages and thereby high luminescence quantum efficiencies with good fill factors and efficient charge extraction.[13] As shown in **Figure 1**a, high open-circuit voltages relative to the bandgap have been shown in halide perovskite solar cells so far mainly for the range of bandgaps of 1.5 to 1.65 eV. For wider bandgaps, approaching the radiative limit has so far been less successful due to increased recombination losses.[14,15] This is unfortunate, because in particular the bandgaps around 1.7 to 1.8 eV are highly relevant for making efficient tandem cells based on low bandgap absorbers such as Si,[16–19] Cu(In,Ga)Se_2[20,21] or Sn-based low bandgap perovskites.[22,23] One reason for the increased recombination losses for wider bandgap absorbers is halide segregation that leads to stability problems for perovskites containing higher concentrations of Br than about 20%.[24–27] Another obvious but less discussed challenge is the choice of electron and hole transport materials that have to be adapted to the energy levels of the absorber material.[10,12,28,29]

Achieving high open-circuit voltages in perovskite solar cells not only requires well passivated surfaces but also the right choice of charge transfer layer (CTL) for a good energy level alignment.[12] In inverted (anode-illuminated) perovskite solar cells, fullerenes are nearly always used as electron transport layers and high efficiency solar cells with fullerene electron transport layers based on C_{60}[30,31] and [6,6]-phenyl-C_{61}-butyric acid methyl ester (PCBM) have been demonstrated for a range of bandgaps.[4,32–38] However, fullerenes have also restrictions in so far that their energy levels cannot easily be tuned over a wide range. The electron affinity of fullerenes changes with the number and type of adducts attached to the C_{60} cage with multiadducts leading to lower electron affinities relative to monoadducts such as PCBM or even C_{60}.[39–41] For instance, for the classical $MAPbI_3$ composition, PCBM provided a good band alignment, while C_{60} (higher electron affinity) leads to additional recombination losses.[42] For higher bandgap perovskites with lower perovskite electron affinities, the lowest-unoccupied molecular-orbital (LUMO) of PCBM becomes too low (electron affinity too high) to achieve a perfect band alignment.[43] However, alternatives such as the indene-C_{60} bisadduct (ICBA) with higher-lying LUMO[28,43,44] suffers from increased energetic disorder due to the high number of isomers (i.e., there are many different ways of attaching two indene groups to one C_{60} cage). This increased disorder leads to a lower

Dr. Z. Liu, J. Siekmann, Dr. B. Klingebiel, Prof. U. Rau, Prof. T. Kirchartz
IEK5-Photovoltaik
Forschungszentrum Jülich
Jülich 52425, Germany
E-mail: j.siekmann@fz-juelich.de; t.kirchartz@fz-juelich.de
Prof. T. Kirchartz
Faculty of Engineering and CENIDE
University of Duisburg-Essen
Carl-Benz-Str. 199, Duisburg 47057, Germany
The ORCID identification number(s) for the author(s) of this article can be found under https://doi.org/10.1002/aenm.202003386.

DOI: 10.1002/aenm.202003386

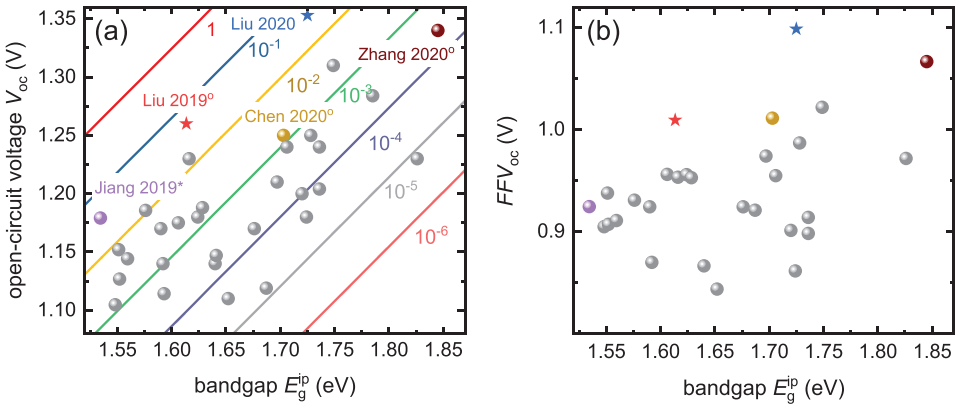

Figure 1. a) Open-circuit voltages V_{oc} versus bandgap. The gray spheres giving an overview of the broad spectrum of different bandgap perovskites. The bandgaps were calculated by the inflection point of the external quantum efficiency. The lines show the external luminescence quantum efficiency (10^{-6}–1) calculated with a step function. The red star represents the result of Liu et al.[4] the blue star is the device with the highest V_{oc} of our series with electron transport layer of CMC:ICBA. b) Product of the fill factor and open-circuit voltage $FF \times V_{oc}$ versus bandgap. We used the down sweep for our best cell with FF = 81.2% and V_{oc} = 1.35 V leading to a product of $FF \times V_{oc}$ = 1.096 V.

mobility[44,45] and has previously led to a generally worse electronic properties in organic polymer:fullerene solar cells.[46–49] Therefore, it is currently unclear how to design the electron transport material for perovskite absorbers with a wider range of bandgaps.

Figure 1a shows the V_{oc} versus the bandgap of a variety of perovskite solar cells. The colored lines represent the external luminescence quantum efficiency $Q_{e,lum}$ that the solar cells need to have to fulfil the relation[50]

$$q\left(V_{oc}^{rad} - V_{oc}\right) = q\Delta V_{oc} = -kT\ln\left(Q_{e,lum}\right) \quad (1)$$

with V_{oc}^{rad} the radiative open-circuit voltage, q the elementary charge, k the Boltzmann constant, and T the cell temperature. The bandgaps were all calculated by the inflection point of the external (photovoltaic) quantum efficiency to enable better comparison between the data points.[51,52] The most notable achievements among wide bandgap perovskites are cells based on compositions such as $Cs_{0.2}FA_{0.8}Pb(I_{0.7}Br_{0.3})_3$,[15] $Cs_{0.05}(FA_xMA_y)_{0.95}Pb(I_{0.76}Br_{0.24})_3$,[53] $Cs_{0.17}FA_{0.83}Pb(I_{0.6}Br_{0.4})_3$,[54] and $CsPb(I_{0.75}Br_{0.25})_3$.[55] The bandgaps vary from 1.69[53] to 1.845 eV[55] with efficiencies up to 20.1%, at a bandgap of 1.69 eV and a V_{oc} = 1.21 V.[53] The V_{oc} fill factor (FF) product, a proxy for the voltage at the maximum power point, plotted as a function of E_g for the same devices is shown in Figure 1b. The device by Zhang et al.[55] shows a high V_{oc} and high V_{oc} FF product, but a large voltage loss ΔV_{oc}. By applying Equation (1) we can estimate the external luminescence quantum efficiency of the solar cell[55] to be $Q_{e,lum} \approx 0.25\%$. It is important to stress that due to additional recombination at interfaces to charge transfer layers, the calculated $Q_{e,lum}$ of the devices is much smaller than the external luminescence quantum efficiency of well passivated perovskite films, exceeding $Q_{e,lum}$ = 35%.[8,56]

In contrast to Zhang et al.,[55] the champion device that is reported in this work (blue star) shows low voltage losses leading to high luminescence quantum efficiency $Q_{e,lum} \approx 5\%$ which is comparable with low bandgap devices like Jiang et al.[3] (violet) and Liu et al.[4] (red star) (see Figure 1a). Furthermore, the champion device shows a high V_{oc} FF product exceeding 1.09 V (see Figure 1b). The corresponding solar cell is based on a methylammonium lead iodide-bromide absorber prepared using lead-acetate ($Pb(CH_3COO)_2$), methylammonium iodide (MAI), and methylammonium bromide (MABr) as precursors. This absorber layer is combined with poly(triaryl amine) (PTAA) as a hole transport layer (HTL) and different combinations of fullerenes with varied LUMO as electron transport layers (ETLs). We test three different fullerenes, namely, PCBM, CMC (C_{60}-fused N-methylpyrrolidine-m-C_{12}-phenyl),[57,58] and ICBA and all binary combinations of these as ETLs. ICBA is known to have a roughly 200 meV[59] lower electron affinity as compared to PCBM and has therefore previously been used in higher bandgap perovskites.[28] CMC is also a monoadduct fullerene but with a longer side chain and has been reported to have a slightly higher electron affinity (40 meV) than PCBM.[58] While we find high open-circuit voltages >1.29 V for all of these ETLs, substantial differences in all device parameters are still observed. We find that the best efficiencies up to 18.9% and open-circuit voltages up to 1.35 V are possible using a combination of CMC and ICBA to form a binary layer.

2. Results

2.1. Device Performance

For optimizing wide bandgap $CH_3NH_3Pb(I_{0.8}Br_{0.2})_3$ layers grown on PTAA for highest possible open-circuit voltage, lead acetate-based perovskite precursors were chosen because they have been shown[4,60] to yield smooth, low defect-density perovskite layers which enable the highest reported V_{oc} for perovskite layers with a bandgap around 1.6 eV. In order to increase the bandgap of the perovskite layer, we doped 20% MABr into $CH_3NH_3PbI_3$ (MAPI) layer to produce perovskite absorber layers with a wide bandgap of 1.72 eV. For bulk passivation, previous studies have shown that addition of MAI into the perovskite precursor solution can lead to passivation of grain boundaries and substantially increased photoluminescence lifetimes.[61] Furthermore, studies on MAPI-based solar cells have shown that excess MAI results in a smaller electron affinity at the surface of MAPI, which led to better energy alignment and

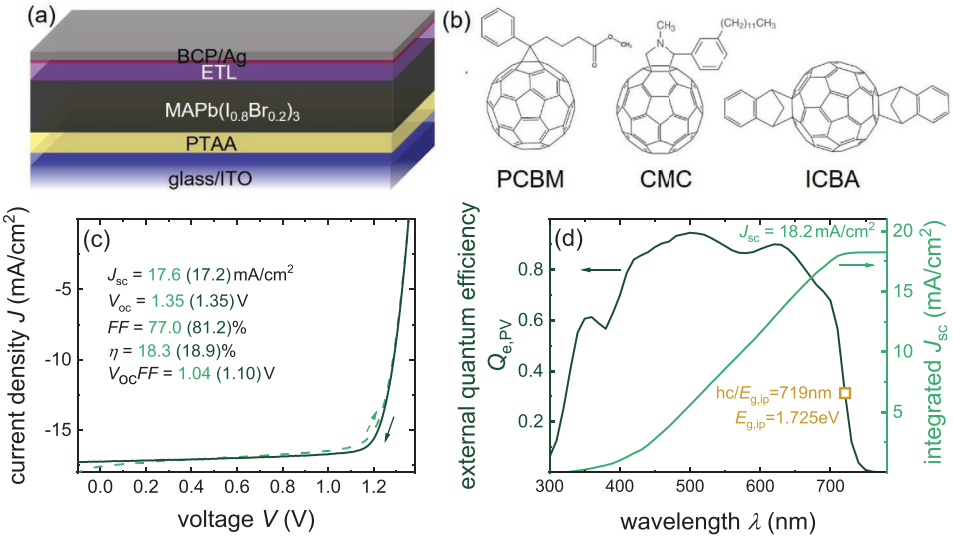

Figure 2. a) Schematic of the device stack. The electron transport layer (ETL) varies between different fullerene derivates and combination of those b) structures of PCBM, CMC, and ICBA. c) Illuminated current–voltage curves of the best device measured four days after production. d) External quantum efficiency $Q_{e,PV}$ of a device on the same sample as our champion cell (Figure S11, Supporting Information). The external quantum efficiency is corrected by the reflection of the cover glass of the sample holder. The integrated J_{sc} = 18.2 mA cm^{-2} is by 1 mA cm^{-2} higher than the measured J_{sc} due to current loss during activation (Figure S9, Supporting Information).

likely an increased built-in voltage in finished devices.[62] Our study shows a continuous improvement in open-circuit voltages when the excess concentration of MAI is increased from 1.67 to 3.33 mol% in $CH_3NH_3Pb(I_{0.8}Br_{0.2})_3$ precursor solution (Figure S4, Supporting Information).

Figure 2a shows a schematic of our device composed of indium tin oxide (ITO), a 16 nm thin PTAA as the hole conductor, $CH_3NH_3Pb(I_{0.8}Br_{0.2})_3$ (≈280 nm) as the absorber, fullerenes shown in Figure 2b (≈25 nm) as the electron transport material, as well as bathocuproine (BCP) (≈8 nm) and Ag (80 nm) finishing up the cathode. Figure 2c shows the current–voltage curve (*JV*) of the champion device, with the blend of CMC and ICBA (1:1, by weight, sic passim) as electron transport layer. The measurements were recorded at a scan speed of 100 mV s^{-1} with a class AAA solar simulator under forward (dashed line) and reverse (solid line) scan conditions. As reported before,[4] in order to reach the high open-circuit voltages, all devices have to be photoactivated either by measuring several current–voltage curves or by being kept under open-circuit conditions for 10–40 min depending on the choice of fullerenes by the white light LED (Figures S2 and S3, Supporting Information). There could be many reasons for the improvement by light soaking. Possible reasons could be strain reduction in the crystal,[63] electronic doping of the fullerene ETLs[64] or movement of the halide ions, leading to defect passivation in the perovskite.[65,66] In this paper we will not further analyze the cause of the activation effect but focus on the electrical and optical characterization of the activated cells and layer stacks. Figure 2d shows the external quantum efficiency of a device on the same sample and with the same short-circuit current as our champion device (Figure S11, Supporting Information). During activation, the J_{sc} slightly decreases causing a 1 mA cm^{-2} difference between the J_{sc} computed by integrating the external quantum efficiency (Figure S9, Supporting Information) and the J_{sc} measured with the solar simulator. It is important to mention that all our cells show an increase in V_{oc} if measured again two days after the first measurement (Figure S5, Supporting Information). Our best cell shows a V_{oc} = 1.35 V measured on day four after production. Cells measured after 4 days lose mostly in J_{sc} (Figure S5, Supporting Information) which could be due to MAI excess of the cells.[62]

2.2. Electron Transport Layer Variations

In order to achieve the high V_{oc}, we varied the type of fullerenes used as ETL. In the following we want to show the impact of different fullerenes and their blends on the characteristic values of the cells. **Figure 3**a,c shows the illuminated *JV*-curves of the best devices, all reaching V_{oc} > 1.29 V. The statistical data in Figure 3b gives a brief overview of the impact of different ETLs on the cell performance, divided in (from left to right, top to bottom) J_{sc}, V_{oc}, *FF*, and η for the pure fullerenes and blends. The box contains 50% of the data points, the antenna shows minimum and maximum value, the bar gives the median, and the point is the mean value. The J_{sc} is highest for the cells with PCBM and decreases by mixing with CMC or ICBA. While the cells with pure CMC and ICBA have lower J_{sc}, the CMC:ICBA blend shows a similar high J_{sc} as pure PCBM. The V_{oc} shows the opposite trend, PCBM and its blends reach V_{oc} > 1.33 V while CMC, ICBA, and their blend increase the V_{oc} up to 1.35 V. With regard to J_{sc} and V_{oc} CMC and ICBA behave similar, but looking at the *FF* we notice a reduced performance for ICBA and PCBM:ICBA blend. Surprisingly, the blend of CMC and ICBA results in an increase of *FF* compared to both pure materials, the difference between the mean fill factor for CMC, ΔFF = 3.4%, and for ICBA is even ΔFF = 12.4%. Thus, the V_{oc} *FF* product is highest for CMC:ICBA and—combined with the good J_{sc}—this ETL leads to the highest efficiency η = 18.9%.

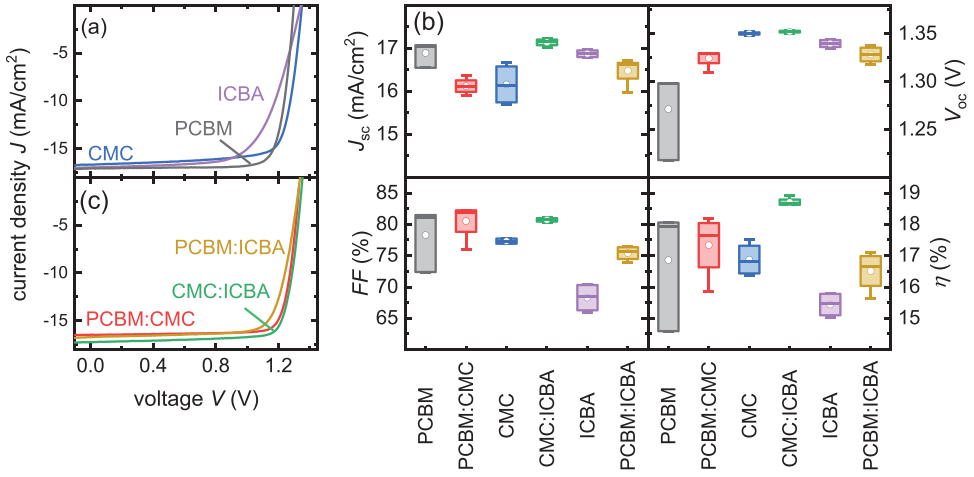

Figure 3. a,c) Illuminated current–voltage curves of cells with different ETLs. Measured on an AAA sun simulator after activation with an LED. b) J_{sc}, V_{oc}, FF, and η statistic of the four cells on one sample. The box contains 50% of the data, the antenna shows minimum and maximum values, the bars give the median (in case of 4 cells the mean value of both median values) and the point gives the mean value.

The other devices reach efficiencies of ≈17% with the exception of the ICBA-based device, where the poor *FF* leads to a low efficiency of $\eta < 16\%$.

Thus, to summarize the findings from Figure 3, we find that the relatively high electron affinity of PCBM indeed leads to the lowest open-circuit voltages in the series, verifying the need for looking into alternative electron transport layer materials. The substitution of PCBM by ICBA enables higher open-circuit voltages thereby verifying the assumption that the energy level alignment at the perovskite–PCBM interface leaves room for improvement.[12] The cells based on ICBA, however, also show a drastically reduced *FF* consistent with the observed charge transport problems of fullerene multiadducts encountered in the past in the context of polymer:fullerene solar cells.[47,48] The apparent solution for this dilemma is found to be the use of the fullerene monoadduct CMC blended in 1:1 ratio with either PCBM or—with even higher efficiencies—ICBA. Thus, the use of binary blends of different fullerenes allows combining their advantages rather than being limited by the shortcomings of the respective molecules. This is an observation that has also previously been made in the context of organic solar cells, where ternary blends using, e.g., two different acceptor molecules combined with one donor have efficiencies that exceed those of the binary blends.[67–69]

2.3. Loss Analysis

In the following, we will briefly study the key loss mechanisms in our solar cells by comparing the performance indicators J_{sc}, V_{oc}, *FF*, and efficiency to the values of a cell with the same bandgap in the Shockley–Queisser model. We use the methodology that has been introduced by Guillemoles et al.[70] and Krückemeier et al.[52]

In **Figure 4**a the power density of our champion device is shown as a function of voltage (blue) and is compared with the power density of a cell with the same bandgap (1.72 eV) with an ideal *FF* (red), ideal V_{oc}, and ideal *FF* (green) and finally the power density–voltage curve of the cell in the Shockley–Queisser model (yellow). Figure 4a emphasizes that we optimized the cells for high V_{oc} and high *FF*. Thus, the difference between ideal J_{sc} and measured J_{sc} is the highest but can be explained by the low absorber thickness of 280 nm that gives the best electronic quality and highest open-circuit voltages. Note that if we use a more highly concentrated precursor solution, the layer thickness increases, but also the crystal growth changes and very rough layers are formed, which are detrimental for the performance of device. The V_{oc} is close to the Shockley–Queisser limit (green curve) for a bandgap of 1.72 eV. As described by Krückemeier et al.[52] a better way to compare the quality of the V_{oc} is by comparing the measured and the radiative open-circuit voltage V_{oc}^{rad}. We calculated V_{oc}^{rad} by fitting an Urbach tail to the external quantum efficiency[52] (Figure 4b). The difference $\Delta V_{oc} = V_{oc}^{rad} - V_{oc} = 70$ mV confirms the good V_{oc} comparable to Liu et al.[4] ($\Delta V_{oc} = 64$ mV) and Jiang et al.[3] ($\Delta V_{oc} = 67$ mV). Notably, this loss is the smallest reported value in the bandgap region around 1.7 eV. Using Equation (1) we can compute an external luminescence quantum efficiency $Q_{e,lum} = 6.56\%$.

Figure 4c shows the ratio of different losses for our champion device with a 1:1 blend of CMC and ICBA and 5 other fullerenes or fullerene blends as ETL. The percentage of SQ efficiency is plotted on a logarithmic axis, i.e., the relative size of the boxes is independent of their position in the total loss bar. The normalized efficiency can be written as

$$\frac{\eta_{real}}{\eta_{SQ}} = \frac{J_{sc}}{J_{sc}^{SQ}} \frac{V_{oc}^{real}}{V_{oc}^{SQ}} \frac{FF_0\left(V_{oc}^{real}\right)}{FF_0\left(V_{oc}^{SQ}\right)} \frac{FF_{real}}{FF_0\left(V_{oc}^{real}\right)} \quad (2)$$

Note that the *FF* depends on the V_{oc}. Hence, the loss in *FF* is divided in the loss in maximum fill factor that is due to the loss in V_{oc}, i.e., $FF_0(V_{oc}^{real})/FF_0(V_{oc}^{SQ})$ (lilac Figure 4c), and the loss in fill factor that is due to the series resistance and the ideality factor $FF_{real}/FF_0(V_{oc}^{real})$ (red Figure 4c). Regardless of the fullerene, the photocurrent loss J_{sc}/J_{sc}^{SQ} (yellow Figure 4c) is the highest loss, which can be partly explained by the small thickness (280 nm) of the absorber layer and no additional light management. All cells show a small loss in calculated *FF* due to a small difference in

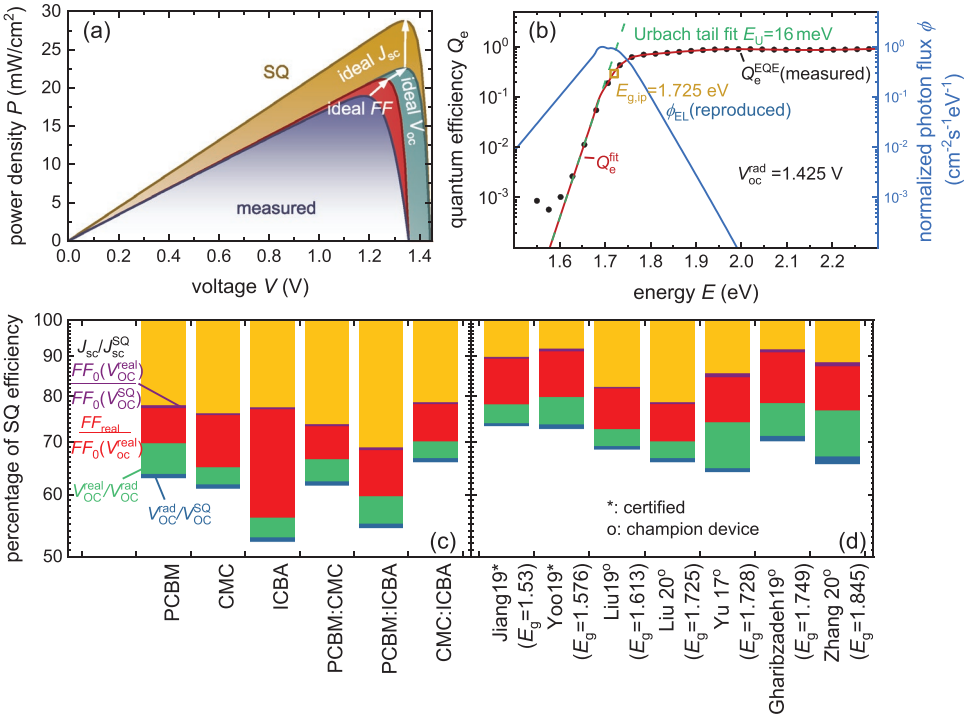

Figure 4. Analysis of losses. a) Power density P of the best cell (blue) compared to the ideal cell in different steps of ideality, ideal fill factor (red), Shockley–Queisser V_{oc} (green), and complete SQ model (yellow). The biggest improvement could be achieved by increasing J_{sc}. b) The radiative limit $V_{oc}^{rad} = 1.42$ V is calculated from the product of photovoltaic quantum efficiency and black body spectrum as described, e.g., by Rau.[50] The photovoltaic quantum efficiency is extended by fitting an Urbach tail of $E_U = 16$ meV to the measured quantum efficiency Q_e^{EQE}as explained by Krückemeier et al.[52] Because the V_{oc}^{rad} should be independent of the ETL, we show the data from the cell with the CMC:ICBA blend as ETL. c) The percentage of Shockley–Queisser efficiency for cells with different ETLs separated in current loss (J_{sc}/J_{sc}^{SQ}), fill factor losses ($FF_{real}/FF_0(V_{oc}^{real})$, $FF_0(V_{oc}^{real})/FF_0(V_{oc}^{SQ})$), and radiative and nonradiative voltage loss (V_{oc}^{rad}/V_{oc}^{SQ}, $V_{oc}^{real}/V_{oc}^{rad}$). d) Percentage of Shockley–Queisser efficiency for perovskite cells with different bandgaps.

V_{oc}^{SQ} and measured V_{oc}. The resistive loss in FF varies for the different ETL. In case of ICBA $FF_{real}/FF_0(V_{oc}^{real})$ is particularly high suggesting a reduced conductivity of the ICBA layer. The loss in V_{oc} can be divided in the difference between the actual absorption coefficient and the assumed step function in SQ (blue Figure 4c) and nonradiative loss (green Figure 4c). The perovskite and thus the bandgap and shape of the external quantum efficiency spectrum in the region close to the bandgap is not severely affected and hence the ratio V_{oc}^{rad}/V_{oc}^{SQ} is nearly the same for all cells. The ratio $V_{oc}^{real}/V_{oc}^{rad}$ is highest for cells which contain PCBM in the ETL and lowest for cells with either ICBA, CMC or ICBA:CMC as ETL. Our champion device based on the CMC:ICBA blend ETL shows a moderate normalized efficiency $\eta_{real}/\eta_{SQ} = 0.66$, but our nonradiative V_{oc} loss is comparable with high efficiency devices based on much lower bandgaps, e.g., Jiang et al.[3] Figure 4d illustrates the exceptionally low voltage losses of our solar cells compared to the voltage losses in other wide bandgap perovskite devices that typically exceed those of lower bandgap perovskites.[15,55,71,72]

2.4. Interfacial Recombination

The most obvious finding from our previous analysis of device data is the observation of high open-circuit voltages and low nonradiative recombination losses. This implies that our process yields a high-quality bulk material which only shows minimal losses due to interface recombination. Interface recombination is affected both by the energy-level alignment[73–75] at the interface between absorber and both charge transport layers and by its kinetics that are typically expressed in terms of surface- or interface-recombination velocities.[76] Here, we will first study the kinetics of recombination using transient photoluminescence measurements and subsequently the energy-level alignment of the different fullerenes by a combination of ultraviolet photoelectron spectroscopy (UPS) and photothermal deflection spectroscopy (PDS).

2.4.1. Recombination Kinetics

We measured transient photoluminescence with time-correlated single-photon counting on half cells without the BCP and silver contact with the decays being shown in **Figure 5**a and b. This was done to reduce the impact of capacitive effects that would be expected from electrode charging and discharging in complete devices.[77] In order to analyze the data, we calculate the differential decay time by first fitting the Tr-PL decays and then differentiating the fits using

$$\tau_{diff,HLI} = -2\left(\frac{d\ln(\phi)}{dt}\right)^{-1} \quad (3)$$

where ϕ is the luminescence. The factor of 2 originates from the assumption of high-level injection (HLI), i.e., $\phi \propto n^2$[78]

where n is the charge-carrier concentration. The resulting differential decay times are plotted as a function of the quasi Fermi-level splitting ΔE_F which is proportional to $\ln(\phi)$ as computed in Equation (S5) of the Supporting Information. Note that early times after the pulse correspond to high ΔE_F and late times to low ΔE_F. The differential decay times as shown in **Figure 5**c,d. show a rapidly decreasing decay time toward high quasi Fermi-level splitting (short times), and a small decrease at intermediate values of ΔE_F. At smaller values of ΔE_F (long times) the decay times differ for the different fullerenes. Decay times for CMC:ICBA (green) and PCBM:ICBA (gold) nearly saturate in a slightly sloped plateau, PCBM (gray) and ICBA (lilac) continue decreasing but with a smaller slope, PCBM:CMC (red) saturates after a steep rise and CMC (blue) increases fast. It should be mentioned that the steady-state PL shows a peak shift (Figure S13, Supporting Information) for PCBM:CMC, which could be the reason for the difference to the other mixed fullerenes. The peak shift could be related to phase segregation during the activation of the sample.[24,25] The decays are generally comparably slow as those measured on similar MAPI samples as presented, e.g., by Liu et al.[4] and Haddad et al.[76]

The first regime of the decay time versus ΔE_F plot (short times) can be affected by charge extraction to the charge transport layers and the ITO electrode as well as by radiative and Auger recombination, leading to relatively short decay times.[78,79] The intermediate and late regime should be dominated by either bulk or interface recombination with an approximately constant lifetime, i.e., some type of defect-assisted SRH process.[80] In contrast to the other fullerenes and blends the differential decay time of CMC increases even further toward lower values of ΔE_F (long times), representing the flat parts of the Tr-PL decays shown in Figure 5a. These regimes are representative of the part of the original data with the lowest signal-to-noise ratio, where the Tr-PL data approaches its background (noise) level. For the other ETLs, we cut off the regime with lowest signal-to-noise ratio as described in Figure S16 of the Supporting Information. In addition, the long-time regime can be affected by slow processes such as capacitive discharges of electrodes or contact layers that reinject charge into the perovskite absorber.[77,80] Therefore, we conclude that the region most representative of the information of interest, namely, all types of SRH recombination, is the flat or intermediate region. If we analyze the data of the 1:1 blend of CMC and ICBA at the point

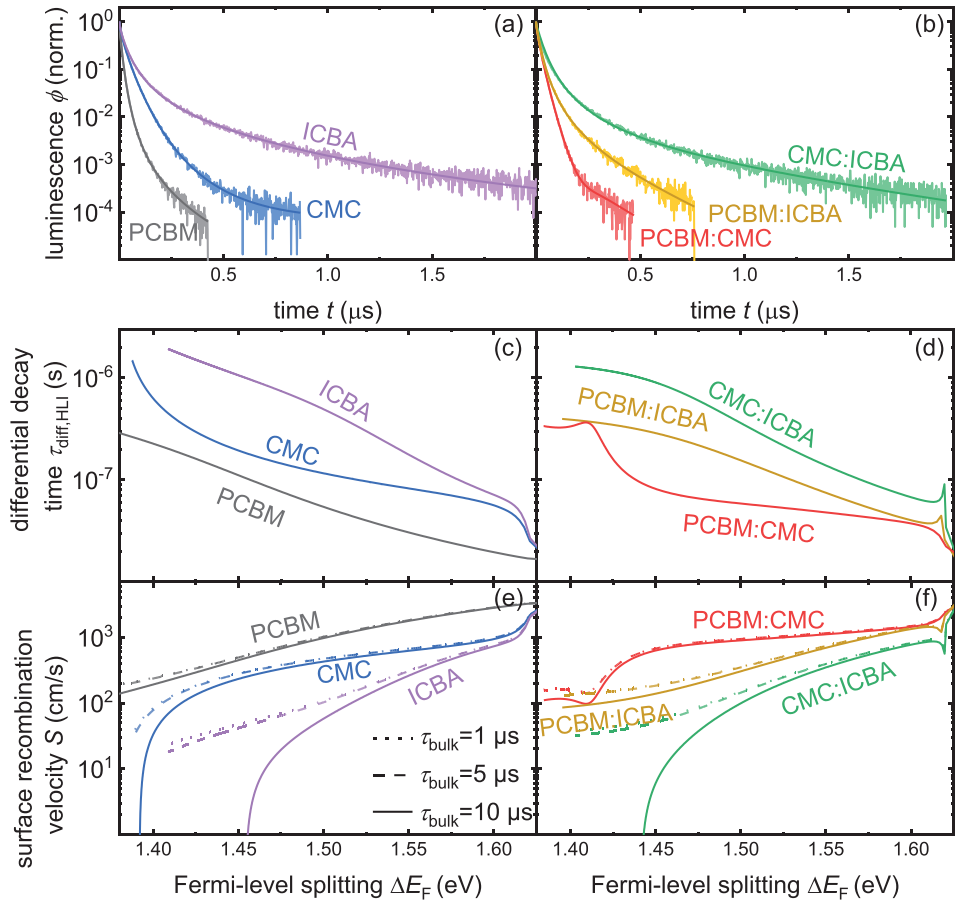

Figure 5. a) Normalized transient photoluminescence ϕ of glass/ITO/PTAA/perovskite/ETL samples with pure and b) mixed fullerenes measured with time correlated single-photon counting (TCSPC). In order to analyze the data, we fit two exponential functions to the normalized data (darker lines). c,d) We computed the differential decay time $\tau_{diff,HLI}$ by using Equation (3) and plotted the result versus Fermi-level splitting ΔE_F. Samples using an ETL made from a (1:1) blend of CMC and ICBA show the highest lifetime of $\tau > 1$ µs. e,f) Surface-recombination velocity S computed with Equation (3) for bulk lifetime τ_{bulk} = 10 µs (dotted line), 5 µs (dashed line), and 1 µs (solid line).

where the derivative of the differential decay time has a minimum, we obtain differential decay times of $\tau_{diff,HIL} \approx 0.75$ µs at $\Delta E_F = 1.46$ eV. As described in Section S5.2 of the Supporting Information, we can estimate surface-recombination velocities from these decay times via

$$S(\Delta E_F) = 2d\left(\frac{1}{\tau_{diff,HLI}(\Delta E_F)} - \frac{1}{\tau_{bulk}}\right) \quad (4)$$

and obtain values ranging from $S = 17$ up to 67 cm s^{-1}. We vary the assumed bulk recombination time from $\tau_{bulk} = 1$, 5, and 10 µs[56] and use a thickness $d = 280$ nm (Figure 5e,f). Especially for ICBA and CMC:ICBA, a bulk lifetime $\tau_{bulk} < 1$ µs would be inconsistent with the long differential decay times, which therefore implies that the value for S computed from Equation (4) becomes extremely low or even negative. In the latter case, the assumed bulk lifetime must be unphysical and a longer lifetime has to be assumed. The values of the surface-recombination velocity presented here are slightly higher than what was previously estimated for the PTAA/MAPI interface[4] based on Tr-PL measurements but slightly lower than previous estimates[76,79] for recombination at the MAPI/PCBM interface. The surface-recombination velocity of PCBM in the assumed bulk lifetime range is nearly one order of magnitude higher than S for CMC:ICBA. Furthermore the combination of PCBM and CMC results in a similarly high S while the ICBA in PCBM:ICBA seems to compensate the PCBM. Note that the effect of the variation of the bulk lifetime is particularly important for cases, where the differential decay time is rather long. Thus, for ICBA and CMC:ICBA, there is a substantial variation in the estimated value of S with τ_{bulk}, while for the other ETLs, there are only minor variations.

2.4.2. Energy Level Alignment and V_{oc} Losses

In addition to surface quality the energy alignment between perovskite and CTL limits the V_{oc}.[12,76] Large offsets, e.g., in the conduction band at the absorber–ETL interface would lead to an interfacial bandgap at this interface that is substantially lower than the bulk bandgap. If recombination is efficient via the interface (i.e., electrons in the ETL can efficiently recombine with holes in the perovskite), the interface may strongly deteriorate the V_{oc}.[62] Therefore, characterization of energy levels is crucial for a complete understanding of interfacial recombination in a solar cell. Typically, UPS is used to measure the work function Φ and the valence-band edge E_v at the surface of the samples. Given that we are interested in the LUMO positions of our ETLs, we have to combine UPS data with data from optical spectroscopy to obtain the bandgap and thereby the electron affinity χ.

We derived the work function and the valence-band edge with UPS measurements as shown in Figure S19 of the Supporting Information for all fullerenes and blends on glass/ITO/PTAA/perovskite/ETL stacks. We activated the half cells before the UPS measurement by illumination under a white LED lamp as described in the Supporting Information. **Figure 6**c illustrates the difference between the ionization energy $E_i = E_{vac} - E_V$ of PCBM and the other fullerenes. We determined a smaller E_i for ICBA of 160 meV, which is in good agreement with the offset (200 meV) measured by Faist et al.[59] The relevant quantity for band alignment with the perovskite is however the electron affinity as it determines electron extraction and recombination of electrons in the ETL with holes in the perovskite. However, fullerenes do not show a clear absorption onset that could be used to determine the bandgap but feature a weakly absorbing absorption feature at around 1.75 eV and then a slow rise

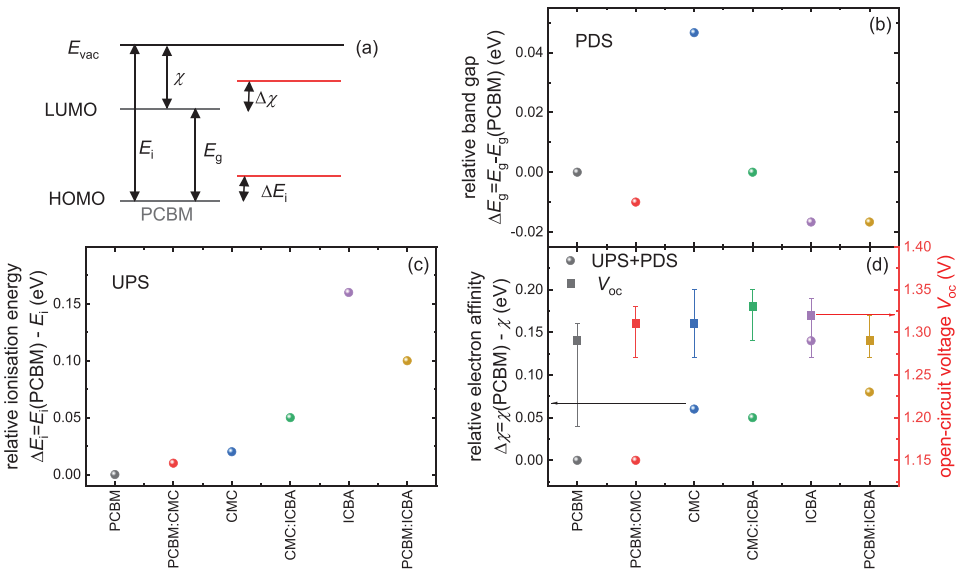

Figure 6. a) Schematic band diagram of PCBM compared to the other ETLs. b) Bandgap difference ΔE_g between PCBM and the other ETL materials, measured with PDS and total transmittance and reflectance spectroscopy. c) Ionization energy $E_i = E_{vac} - E_V$ relative to the ionization energy of PCBM. The work function Φ and the valence band energy relative to the Fermi-level energy $E_F = 0$ eV were derived from UPS measurements. d) Difference between electron affinity of PCBM and the other ETLs. The electron affinity was computed with the PDS measurements and UPS measurements and the median V_{oc} with the error bar representing the datapoints within 1.5 × IQR (Figure S12, Supporting Information).

until strong absorption is visible in the blue and UV parts of the spectrum. This has led to substantial variations of electron affinities determined by combining UPS and absorption spectroscopy in literature.[45,58,81–84] In order to circumvent this challenge, we again only compare relative changes in bandgap that we determine from PDS measurements analyzed at three different constant absorption coefficients $\alpha = 1 \times 10^4\,\mathrm{cm}^{-1}$, $\alpha = 5 \times 10^3\,\mathrm{cm}^{-1}$, and $\alpha = 1 \times 10^3\,\mathrm{cm}^{-1}$. The arithmetic means of the three optical bandgap differences with respect to PCBM are shown in Figure 6b. We observe that the optical bandgap of CMC is ≈ 40 meV bigger than the bandgap of PCBM while the other fullerenes show slightly lower bandgaps than PCBM.

Figure 6d shows the relative position of the LUMO of the different ETLs compared to PCBM determined from the values in Figure 6b,c and the median V_{oc} from the solar cell characterization. The error bars of V_{oc} represent the datapoints within 1.5 × IQR (interquartile range), where the IQR represents the region of 50% of the data points (Figure S10, Supporting Information). PCBM and PCBM:CMC share the same electron affinity, while the other blends and fullerenes have a lower electron affinity. The LUMO of ICBA is closest to vacuum, fitting to the high V_{oc}. However, the correlation between V_{oc} and $\Delta\chi$ is not distinct enough to solely explain the high V_{oc}. Instead, we propose that the combination of the optimization of the energy level alignment and slight improvements in the interface passivation suggested by the Tr-PL measurements qualitatively explain the trends in V_{oc}. A quantitative prediction of the trends of V_{oc} with ETL may be a target for future studies but has so far not been attempted due to the difficulties in the numerical simulations of Tr-PL decays and the experimental uncertainties in measuring energy level alignment with accuracies of a tens of mV.

2.5. Fill Factor Losses

As observed in Figure 4c,d, the fill factor losses are still substantial and even at fill factors ≈ 80% generally exceed the losses in V_{oc} in the cells discussed here. The same is true for most high efficiency perovskite solar cells reported in literature and stands out relative to more mature technologies such as Si or GaAs where these losses are substantially lower.[52] These losses partly originate from the high ideality factors observed even in high efficiency perovskite solar cells[13,85] and from the resistive losses induced by the relative low conductivity and low permittivity of the organic charge transport layers.[86] In the following, we will therefore study the general distribution of *FF* losses in more detail and analyze in particular resistive losses due to low mobilities in the ETLs via space-charge-limited current (SCLC) measurements.

2.5.1. Analysis of Current–Voltage Curves

In order to distinguish between resistive contributions to the fill factor loss and those based on an ideality factor n_{id} higher than one, we use a simple method to determine the series resistance R_s by comparing illuminated and dark *JV*-curve in the 4th quadrant.[87,88] When neglecting the parallel resistance and assuming the superposition principle[89,90] holds, the diode equation

$$J_l = J_0 \times \left(\exp\left(\frac{q(V_l - J_l R_s)}{n_{id} kT} \right) - 1 \right) - J_{sc} \tag{5}$$

with k the Boltzmann constant and T the cell temperature and $J_0 = J_{sc} \times \exp(-qV_{oc}/kT)$ describes the *JV*-curve of a solar cells. In the dark the diode equation is reduced to

$$J_d = J_0 \times \left(\exp\left(\frac{q(V_d - J_d R_s)}{n_{id} kT} \right) - 1 \right) \tag{6}$$

where the *JV*-curve is independent of light induced effects. The J_{sc}/V_{oc} curve, i.e., J_{sc} and V_{oc} measured at different illumination intensities is independent of R_s

$$J_{sc} = J_0 \times \left(\exp\left(\frac{qV_{oc}}{n_{id} kT} \right) - 1 \right) \tag{7}$$

since the current is zero at V_{oc}. **Figure 7**a shows the illuminated *JV* curve (blue) the dark *JV* curve shifted by J_{sc} (yellow), the J_{sc}/V_{oc} curve shifted by J_{sc} (red) and the ideal *JV* curve (green), i.e., $R_s = 0\,\Omega\,\mathrm{cm}^2$ and $n_{id} = 1$ for a PCBM cell. For equal current densities *J*, the difference between illuminated *JV* curve and dark *JV* curve divided by J_{sc} leads to the series resistance[91]

$$R_S = (V_d - V_l)/(J_d - J_l) = (V_d - V_l)/J_{sc} \tag{8}$$

as long as the series resistance is independent of illumination intensities (Figure 7c). The mean series resistance for the PCBM cell is $R_s \approx 5.4\,\Omega\,\mathrm{cm}^2$ in a voltage range of $V_d \approx 1.24$ to 1.36 V (being very similar for forward and reverse scan) and increases toward lower voltage due to the increased internal resistance of the semiconducting layers making up the device.[87] Note that the series resistance can as well be calculated by the difference between illuminated *JV* curve and J_{sc}/V_{oc} curve, dark *JV* curve, and J_{sc}/V_{oc} curve,[87] respectively. The latter two approaches are however more prone to hysteresis effects as discussed in more detail in Section S7.2 of the Supporting Information. According to Green's equation for the fill factor,[92] it depends not only on the series resistance but also on the ideality factor n_{id}. Therefore, we determine the ideality factor by calculating the slope of the short-circuit current plotted against the open-circuit voltage at different illumination intensities (Figure 7b; Figure S26, Supporting Information). The ideality factor for PCBM is in the range of roughly $n_{id} \approx 1.7$ to 1.9 for the reverse scan direction and even higher in the forward scan. In Figure 7d we plotted the power density versus voltage for the different *JV* curves in a similar manner to Figure 4a. The maximum of the power density curve gives us the efficiency of our solar cell. The difference between illuminated and J_{sc}/V_{oc} curve reveals the fill factor loss $\Delta FF_{R_s} = FF_{J_{sc}V_{oc}} - FF_l = 3.7\%$ due to the series resistance in the cell. The difference between J_{sc}/V_{oc} curve and ideal power density curve gives us the loss due to nonideal diode behavior, i.e., an ideality factor $n_{id} > 1$.[93] The fill factor loss due to nonideal diode behavior is slightly larger than the loss due to R_s $\Delta FF_{n_{id}} = FF_{id} - FF_{J_{sc}V_{oc}} = 5.9\%$ (see **Table 1**).

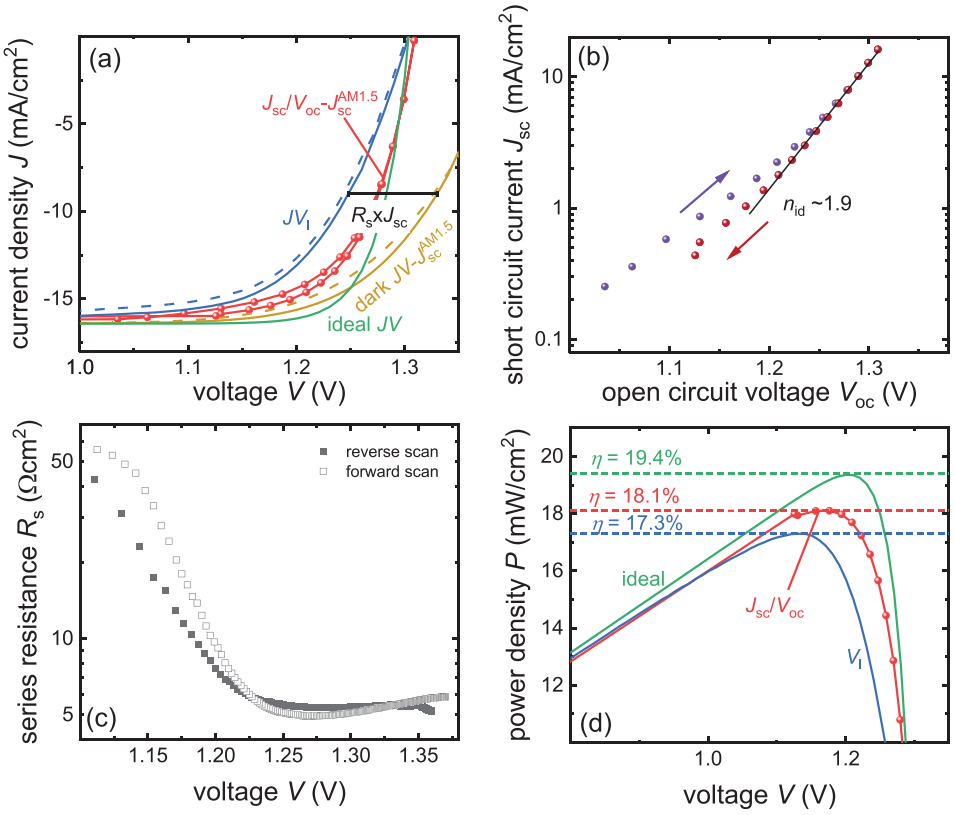

Figure 7. a) Illuminated current–voltage curve (blue) forward (dashed line) and reversed (solid line) scan direction, of a PCBM cell measured with an AAA sun simulator. Short-circuit current density versus open-circuit voltage measured on a white LED subtracted by the short-circuit density at 1 sun $J_{sc}^{AM1.5}$ (red). Dark *JV* curve subtracted by $J_{sc}^{AM1.5}$ (green) and ideal *JV* curve following Equation (5). b) Short-circuit current plotted against open-circuit voltage of the PCBM cell at different light intensities. The upsweep (low intensity to high intensity) is shown in purple and the downsweep (high intensity to low intensity) in red. c) The difference between illuminated *JV* and dark *JV* leads to the series resistance R_s following Equation (8). The open symbols represent the difference between the forward scans of illuminated and dark curves, the filled symbols the reverse scan, respectively. d) Power density of the illuminated, J_{sc}/V_{oc} and ideal curve. The maximum power density is equal to the efficiency of the solar cells.

2.5.2. Space-Charge-Limited Current Measurements

The observation of improved *FF* for the binary ETLs compared to pure fullerene ETLs as shown in Figure 3d, suggests that the choice of fullerene or fullerene blend affects the conductivity of the ETL which in turn could modulate the resistive losses caused by the ETL. Hence, we studied the difference in electron mobility μ_e across the different ETLs using SCLC measurements. Therefore, we constructed electron only devices, similar to the cell stack. As shown in **Figure 8**a, we used ZnO nanoparticles and the standard BCP/Ag contact also used in the solar cells as electron injecting and extracting contact for the electron-only devices. In SCLC measurements, the current should follow the Mott–Gurney law[94]

$$J = \frac{9}{8}\varepsilon_0\varepsilon_r\mu_e\frac{V^2}{d^3} \tag{9}$$

where ε_0 is the vacuum permittivity, $\varepsilon_r = 3$ is the assumed relative permittivity, and d is the thickness of the fullerenes and fullerene blends if certain conditions are met. These conditions include most notably the absence of diffusion—an assumption that is typically violated if there are either charged defects or asymmetric injection barriers present in the device. In order to distinguish between both effects, we measured the dark *JV* curve from −4 to 4 V with the difference between forward and reverse bias being indeed substantial (see Figure S21, Supporting Information).[95,96] To minimize the influence of diffusion on the data, we use the curve obtained by injecting electrons at the BCP/Ag electrode and extracting them at the ZnO electrode and limit ourselves to voltages $V > 1$ V.

Figure 8a shows a double-logarithmic representation of this part of the data shown as $J \times d^3$ versus voltage showing a transition from a region affected by diffusion to a region that is approximately following the Mott–Gurney law for higher

Table 1. J_{sc}, V_{oc}, *FF*, and η for a solar cell based on an PCBM ETL compared to FF and η from an ideal *JV* curve with the same J_{sc} and V_{oc} but $R_s = 0$ and $n_{id} = 1$ and a curve with zero series resistance (but nonideal n_{id}), derived from the measurement of the J_{sc}/V_{oc} curves shown in Figure 8a,b.

	J_{sc} [mA cm^{-2}]	V_{oc} [V]	FF_I [%]	FF_{JscVoc} [%]	FF_{id} [%]	η [%]	η_{JscVoc} [%]	η_{id} [%]	ΔFF_{R_s} [%]	$\Delta FF_{n_{id}}$ [%]
PCBM	16.4	1.30	81.1	84.8	90.7	17.3	18.1	19.4	3.7	5.9

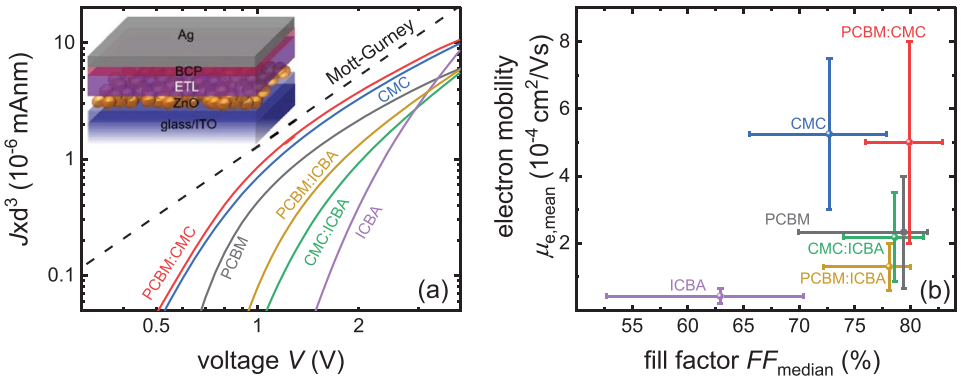

Figure 8. a) Space-charge-limited current (SCLC) $J \times d^3$ versus voltage for the bias direction where electrons are injected from the BCP/Ag and extracted at the ZnO interface. (Comparison between forward and reverse direction can be found in Figure S21, Supporting Information.) For high voltages, the curve should follow the Mott–Gurney law (Equation (4)) Inset: schematic of the electron-only device stack using BCP/Ag und ZnO as the electron injecting materials. b) Electron mobility from ASA simulation (see the Supporting Information) plotted against the median FF of all cells measured with AAA sun simulator on day four. The error bar for the mobility represents the uncertainty in thickness due to surface roughness. The error bar of FF represents the datapoints within 1.5 × IQR (Figure S12, Supporting Information).

voltages. Note that assuming constant permittivity among the different fullerenes, higher values of $J \times d^3$ should always correspond to higher mobilities according to Equation (9). The Mott–Gurney law can only be applied in the region where the slope in the double log plot is close to two.[97] All samples except the ICBA-based sample show a transition from a high slope at lower voltages (diffusion limited region) to a smaller slope at higher voltages that approaches the value of 2 expected from the Mott–Gurney law. The curves for the different fullerenes are approximately parallel suggesting that they differ essentially in mobility. On the contrary the ICBA-based sample shows a substantially higher slope than 2 throughout the whole voltage region suggesting that energetic disorder affects charge transport.[98] Figure 8a leads to the conclusion that PCBM:CMC and CMC have the highest mobility while ICBA shows the lowest mobility of all six fullerenes and—given the higher slope of current versus voltage—is affected by energetic disorder.[98]

To extract the mobility, we simulated the complete *JV* curve with the drift-diffusion simulation solver Advanced Semiconductor Analysis (ASA) to compute the mobility as described in Section S7.1 of the Supporting Information. Figure 8b shows the result of numerically fitting the curves and extracting the electron mobility μ_e for the different ETLs. This electron mobility is then plotted as a function of *FF*. The ZnO nanoparticles form a rough layer which leads to uncertainties in the thickness of the fullerene layers that are reflected in the error bar of the mobility. The fill factor is the median of all measured cells at an AAA sun simulator on day 4 after activation, while the error bars represent 1.5 × IQR. With the exception of the CMC sample that shows a fairly good mobility relative to a modest *FF*, we observe a monotonous increase of *FF* with electron mobility from ICBA (worst *FF*) to PCBM:CMC (best *FF*). 1D-drift-diffusion simulations of *JV* curves (Figure S23, Supporting Information) confirm the electron mobility trend shown in Figure 8b for all ETLs but CMC. Note that the CMC sample is inhomogeneous (Figure S24, Supporting Information), thus the thickness measurements may have a larger error bar, or the material properties could be different to those properties present in a cell with much thinner CMC layer.

3. Conclusion

Reaching high open-circuit voltage is one of the main challenges for wide bandgap perovskite solar cells. Using $CH_3NH_3Pb(I_{0.8}Br_{0.2})_3$ with a bandgap of E_g = 1.72 eV and a blend of CMC:ICBA as electron transport layer we managed to fabricate solar cells with a high V_{oc} = 1.35 eV leading to a nonradiative loss of only ΔV_{oc} = 70 mV without compromising in *FF* = 81.2%. Using transient photoluminescence spectroscopy and a combination of ultraviolet photoelectron spectroscopy and photothermal deflection spectroscopy, we were able to assign the high V_{oc} to low interfacial recombination and partly improved energy alignment. In addition, we studied the losses in fill factor, which are substantial given that corresponding *FF* in the SQ model is nearly 91% for a V_{oc} of 1.35 V. By using a comparison of measured current–voltage curves and suns-V_{oc} measurements, we find that the *FF* losses are distributed approximately equally between losses due to the ideality factor $n_{id} > 1$ and due to resistive losses. The resistive losses most likely originate from the finite conductivity of the charge transport layers. Space-charge-limited current measurements show that the electron mobility in the ETL materials varies for all fullerenes and fullerene blends, showing a monotonic correlation between *FF* and electron mobility that holds for all samples but one. This suggests that further pathways toward higher efficiencies can be based on higher conductivities and mobilities in the electron transport layers combined with a better understanding of ideality-factor losses. The latter losses may be reduced by either further approaching the radiative limit for example by better surface quality or by moving the most recombination active parts of the device into low level injection.

Supporting Information

Supporting Information is available from the Wiley Online Library or from the author.

Acknowledgements

Z.L. and J.S. contributed equally to this work. The authors acknowledge support from the Helmholtz Association for funding via the PEROSEED project. Z.L. and J.S. want to thank Oliver Thimm for the PDS measurements. The authors also thank the Initiative and Networking Fund of the Helmholtz Association for funding of the JOSEPH cluster system via the Helmholtz Energy Materials Characterization Platform (HEMCP).

Open access funding enabled and organized by Projekt DEAL.

Conflict of Interest

The authors declare no conflict of interest.

Data Availability Statement

The data that support the findings of this study are available from the corresponding author upon reasonable request.

Keywords

fullerene blends, high open-circuit voltage, low nonradiative recombination, perovskites solar cells, wide bandgaps

Received: October 26, 2020
Revised: February 18, 2021
Published online: March 10, 2021

[1] W. Tress, *Adv. Energy Mater.* **2017**, *7*, 1602358.
[2] J. P. Correa-Baena, M. Saliba, T. Buonassisi, M. Grätzel, A. Abate, W. Tress, A. Hagfeldt, *Science* **2017**, *358*, 739.
[3] Q. Jiang, Y. Zhao, X. Zhang, X. Yang, Y. Chen, Z. Chu, Q. Ye, X. Li, Z. Yin, J. You, *Nat. Photonics* **2019**, *13*, 460.
[4] Z. Liu, L. Krückemeier, B. Krogmeier, B. Klingebiel, J. A. Márquez, S. Levcenko, S. Öz, S. Mathur, U. Rau, T. Unold, T. Kirchartz, *ACS Energy Lett.* **2019**, *4*, 110.
[5] M. Jeong, I. W. Choi, E. M. Go, Y. Cho, M. Kim, B. Lee, S. Jeong, Y. Jo, H. W. Choi, J. Lee, J.-H. Bae, S. K. Kwak, D. S. Kim, C. Yang, *Science* **2020**, *369*, 1615.
[6] H. Lu, Y. Liu, P. Ahlawat, A. Mishra, W. R. Tress, F. T. Eickemeyer, Y. Yang, F. Fu, Z. Wang, C. E. Avalos, B. I. Carlsen, A. Agarwalla, X. Zhang, X. Li, Y. Zhan, S. M. Zakeeruddin, L. Emsley, U. Rothlisberger, L. Zheng, A. Hagfeldt, M. Grätzel, *Science* **2020**, *370*, 8985.
[7] G. Kim, H. Min, K. S. Lee, D. Y. Lee, S. M. Yoon, S. I. Seok, *Science* **2020**, *370*, 108.
[8] I. L. Braly, D. W. deQuilettes, L. M. Pazos-Outon, S. Burke, M. E. Ziffer, D. S. Ginger, H. W. Hillhouse, *Nat. Photonics* **2018**, *12*, 355.
[9] M. Abdi-Jalebi, Z. Andaji-Garmaroudi, S. Cacovich, C. Stavrakas, B. Philippe, J. M. Richter, M. Alsari, E. P. Booker, E. M. Hutter, A. J. Pearson, S. Lilliu, T. J. Savenije, H. Rensmo, G. Divitini, C. Ducati, R. H. Friend, S. D. Stranks, *Nature* **2018**, *555*, 497.
[10] A. Al-Ashouri, A. Magomedov, M. Roß, M. Jošt, M. Talaikis, G. Chistiakova, T. Bertram, J. A. Márquez, E. Köhnen, E. Kasparavičius, S. Levcenco, L. Gil-Escrig, C. J. Hages, R. Schlatmann, B. Rech, T. Malinauskas, T. Unold, C. A. Kaufmann, L. Korte, G. Niaura, V. Getautis, S. Albrecht, *Energy Environ. Sci.* **2019**, *12*, 3356.
[11] M. Stolterfoht, C. M. Wolff, J. A. Márquez, S. Zhang, C. J. Hages, D. Rothhardt, S. Albrecht, P. L. Burn, P. Meredith, T. Unold, D. Neher, *Nat. Energy* **2018**, *3*, 847.
[12] M. Stolterfoht, P. Caprioglio, C. M. Wolff, J. A. Márquez, J. Nordmann, S. Zhang, D. Rothhardt, U. Hörmann, Y. Amir, A. Redinger, L. Kegelmann, F. Zu, S. Albrecht, N. Koch, T. Kirchartz, M. Saliba, T. Unold, D. Neher, *Energy Environ. Sci.* **2019**, *12*, 2778.
[13] M. Stolterfoht, M. Grischek, P. Caprioglio, C. M. Wolff, E. Gutierrez-Partida, F. Peña-Camargo, D. Rothhardt, S. Zhang, M. Raoufi, J. Wolansky, et al., *Adv. Mater.* **2020**, *32*, 2000080.
[14] C. Chen, Z. Song, C. Xiao, D. Zhao, N. Shrestha, C. Li, G. Yang, F. Yao, X. Zheng, R. J. Ellingson, C.-S. Jiang, M. Al-Jassim, K. Zhu, G. Fang, Y. Yan, *Nano Energy* **2019**, *61*, 141.
[15] Y. Yu, C. Wang, C. R. Grice, N. Shrestha, D. Zhao, W. Liao, L. Guan, R. A. Awni, W. Meng, A. J. Cimaroli, K. Zhu, R. J. Ellingson, Y. Yan, *ACS Energy Lett.* **2017**, *2*, 1177.
[16] Z. Yu, M. Leilaeioun, Z. Holman, *Nat. Energy* **2016**, *1*, 16137.
[17] T. Leijtens, K. A. Bush, R. Prasanna, M. D. McGehee, *Nat. Energy* **2018**, *3*, 828.
[18] J. Xu, C. C. Boyd, Z. J. Yu, A. F. Palmstrom, D. J. Witter, B. W. Larson, R. M. France, J. Werner, S. P. Harvey, E. J. Wolf, W. Weigand, S. Manzoor, M. F. A. M. van Hest, J. J. Berry, J. M. Luther, Z. C. Holman, M. D. McGehee, *Science* **2020**, *367*, 1097.
[19] D. Kim, H. J. Jung, I. J. Park, B. W. Larson, S. P. Dunfield, C. Xiao, J. Kim, J. Tong, P. Boonmongkolras, S. G. Ji, F. Zhang, S. R. Pae, M. Kim, S. B. Kang, V. Dravid, J. J. Berry, J. Y. Kim, K. Zhu, D. H. Kim, B. Shin, *Science* **2020**, *368*, 155.
[20] Q. Han, Y.-T. Hsieh, L. Meng, J.-L. Wu, P. Sun, E.-P. Yao, S.-Y. Chang, S.-H. Bae, T. Kato, V. Bermudez, Y. Yang, *Science* **2018**, *361*, 904.
[21] S. Gharibzadeh, I. M. Hossain, P. Fassl, B. A. Nejand, T. Abzieher, M. Schultes, E. Ahlswede, P. Jackson, M. Powalla, S. Schäfer, *Adv. Funct. Mater.* **2020**, *30*, 1909919.
[22] G. E. Eperon, T. Leijtens, K. A. Bush, R. Prasanna, T. Green, J. T.-W. Wang, D. P. McMeekin, G. Volonakis, R. L. Milot, R. May, A. Palmstrom, D. J. Slotcavage, R. A. Belisle, J. B. Patel, E. S. Parrott, R. J. Sutton, W. Ma, F. Moghadam, B. Conings, A. Babayigit, H.-G. Boyen, S. Bent, F. Giustino, L. M. Herz, M. B. Johnston, M. D. McGehee, H. J. Snaith, *Science* **2016**, *354*, 861.
[23] J. Tong, Z. Song, D. H. Kim, X. Chen, C. Chen, A. F. Palmstrom, P. F. Ndione, M. O. Reese, S. P. Dunfield, O. G. Reid, J. Liu, F. Zhang, S. P. Harvey, Z. Li, S. T. Christensen, G. Teeter, D. Zhao, M. M. Al-Jassim, M. F. A. M. van Hest, M. C. Beard, S. E. Shaheen, J. J. Berry, Y. Yan, K. Zhu, *Science* **2019**, *364*, 475.
[24] S. Mahesh, J. M. Ball, R. D. J. Oliver, D. P. McMeekin, P. K. Nayak, M. B. Johnston, H. J. Snaith, *Energy Environ. Sci.* **2020**, *13*, 258.
[25] E. T. Hoke, D. J. Slotcavage, E. R. Dohner, A. R. Bowring, H. I. Karunadasa, M. D. McGehee, *Chem. Sci.* **2015**, *6*, 613.
[26] D. J. Slotcavage, H. I. Karunadasa, M. D. McGehee, *ACS Energy Lett.* **2016**, *1*, 1199.
[27] A. Sadhanala, F. Deschler, T. H. Thomas, S. E. Dutton, K. C. Goedel, F. C. Hanusch, M. L. Lai, U. Steiner, T. Bein, P. Docampo, *J. Phys. Chem. Lett.* **2014**, *5*, 2501.
[28] S. Wheeler, D. Bryant, J. Troughton, T. Kirchartz, T. Watson, J. Nelson, J. R. Durrant, *J. Phys. Chem. C* **2017**, *121*, 13496.
[29] A. Al-Ashouri, E. Köhnen, B. Li, A. Magomedov, H. Hempel, P. Caprioglio, J. A. Márquez, A. B. Morales Vilches, E. Kasparavicius, J. A. Smith, N. Phung, D. Menzel, M. Grischek, L. Kegelmann, D. Skroblin, C. Gollwitzer, T. Malinauskas, M. Jošt, G. Matič, B. Rech, R. Schlatmann, M. Topič, L. Korte, A. Abate, B. Stannowski, D. Neher, M. Stolterfoht, T. Unold, V. Getautis, S. Albrecht, *Science* **2020**, *370*, 1300.
[30] A. Y. Alsalloum, B. Turedi, X. Zheng, S. Mitra, A. A. Zhumekenov, K. J. Lee, P. Maity, I. Gereige, A. AlSaggaf, I. S. Roqan, O. F. Mohammed, O. M. Bakr, *ACS Energy Lett.* **2020**, *5*, 657.
[31] X. Zheng, Y. Hou, C. Bao, J. Yin, F. Yuan, Z. Huang, K. Song, J. Liu, J. Troughton, N. Gasparini, C. Zhou, Y. Lin, D.-J. Xue, B. Chen, A. K. Johnston, N. Wei, M. N. Hedhili, M. Wei, A. Y. Alsalloum, P. Maity, B. Turedi, C. Yang, D. Baran, T. D. Anthopoulos, Y. Han,

Z.-H. Lu, O. F. Mohammed, F. Gao, E. H. Sargent, O. M. Bakr, *Nat. Energy* **2020**, *5*, 131.
[32] Y. Lin, B. Chen, F. Zhao, X. Zheng, Y. Deng, Y. Shao, Y. Fang, Y. Bai, C. Wang, J. Huang, *Adv. Mater.* **2017**, *29*, 1700607.
[33] Y. Shao, Y. Yuan, J. Huang, *Nat. Energy* **2016**, *1*, 15001.
[34] Y. Shao, Z. Xiao, C. Bi, Y. Yuan, J. Huang, *Nat. Commun.* **2014**, *5*, 5784.
[35] D. Luo, W. Yang, Z. Wang, A. Sadhanala, Q. Hu, R. Su, R. Shivanna, G. F. Trindade, J. F. Watts, Z. Xu, *Science* **2018**, *360*, 1442.
[36] C. Zuo, L. Ding, *Adv. Energy Mater.* **2017**, *7*, 1601193.
[37] S. Wu, J. Zhang, Z. Li, D. Liu, M. Qin, S. H. Cheung, X. Lu, D. Lei, S. K. So, Z. Zhu, A. K. Y. Jen, *Joule* **2020**, *4*, 1248.
[38] L. Wan, W. Zhang, S. Fu, L. Chen, Y. Wang, Z. Xue, Y. Tao, W. Zhang, W. Song, J. Fang, *J. Mater. Chem. A* **2020**, *8*, 6517.
[39] Y. He, H.-Y. Chen, J. Hou, Y. Li, *J. Am. Chem. Soc.* **2010**, *132*, 1377.
[40] M. Lenes, G.-J. A. H. Wetzelaer, F. B. Kooistra, S. C. Veenstra, J. C. Hummelen, P. W. M. Blom, *Adv. Mater.* **2008**, *20*, 2116.
[41] H. Wang, Y. He, Y. Li, H. Su, *J. Phys. Chem. A* **2012**, *116*, 255.
[42] C. M. Wolff, F. Zu, A. Paulke, L. P. Toro, N. Koch, D. Neher, *Adv. Mater.* **2017**, *29*, 1700159.
[43] Y. Lin, B. Chen, F. Zhao, X. Zheng, Y. Deng, Y. Shao, Y. Fang, Y. Bai, C. Wang, J. Huang, *Adv. Mater.* **2017**, *29*, 1700607.
[44] P. W. Liang, C. C. Chueh, S. T. Williams, A. K. Y. Jen, *Adv. Energy Mater.* **2015**, *5*, 1402321.
[45] J. Chen, X. Lian, Y. Zhang, W. Yang, J. Li, M. Qin, X. Lu, G. Wu, H. Chen, *J. Mater. Chem. A* **2018**, *6*, 18010.
[46] J. M. Frost, M. A. Faist, J. Nelson, *Adv. Mater.* **2010**, *22*, 4881.
[47] F. Steiner, S. Foster, A. Losquin, J. Labram, T. D. Anthopoulos, J. M. Frost, J. Nelson, *Mater. Horiz.* **2015**, *2*, 113.
[48] M. A. Faist, S. Shoaee, S. Tuladhar, G. F. A. Dibb, S. Foster, W. Gong, T. Kirchartz, D. D. C. Bradley, J. R. Durrant, J. Nelson, *Adv. Energy Mater.* **2013**, *3*, 744.
[49] M. A. Faist, P. E. Keivanidis, S. Foster, P. H. Wöbkenberg, T. D. Anthopoulos, D. D. C. Bradley, J. R. Durrant, J. Nelson, *J. Polym. Sci., Part B: Polym. Phys.* **2011**, *49*, 45.
[50] U. Rau, *Phys. Rev. B* **2007**, *76*, 085303.
[51] U. Rau, B. Blank, T. C. Müller, T. Kirchartz, *Phys. Rev. Appl.* **2017**, *7*, 044016.
[52] L. Krückemeier, U. Rau, M. Stolterfoht, T. Kirchartz, *Adv. Energy Mater.* **2020**, *10*, 1902573.
[53] F. Peña-Camargo, P. Caprioglio, F. Zu, E. Gutierrez-Partida, C. M. Wolff, K. Brinkmann, S. Albrecht, T. Riedl, N. Koch, D. Neher, *ACS Energy Lett.* **2020**, *5*, 2728.
[54] S. Gharibzadeh, B. Abdollahi Nejand, M. Jakoby, T. Abzieher, D. Hauschild, S. Moghadamzadeh, J. A. Schwenzer, P. Brenner, R. Schmager, A. A. Haghighirad, L. Weinhardt, U. Lemmer, B. S. Richards, I. A. Howard, U. W. Paetzold, *Adv. Energy Mater.* **2019**, *9*, 1803699.
[55] J. Zhang, Z. Wang, A. Mishra, M. Yu, M. Shasti, W. Tress, D. J. Kubicki, C. E. Avalos, H. Lu, Y. Liu, *Joule* **2020**, *4*, 222.
[56] D. W. deQuilettes, S. Koch, S. Burke, R. K. Paranji, A. J. Shropshire, M. E. Ziffer, D. S. Ginger, *ACS Energy Lett.* **2016**, *1*, 438.
[57] M. Chikamatsu, K. Kikuchi, T. Kodama, H. Nishikawa, I. Ikemoto, N. Yoshimoto, T. Hanada, Y. Yoshida, N. Tanigaki, K. Yase, *AIP Conf. Proc.* **2001**, *590*, 455.
[58] D. B. Khadka, Y. Shirai, M. Yanagida, T. Noda, K. Miyano, *ACS Appl. Mater. Interfaces* **2018**, *10*, 22074.
[59] M. A. Faist, T. Kirchartz, W. Gong, R. S. Ashraf, I. McCulloch, J. C. de Mello, N. J. Ekins-Daukes, D. D. C. Bradley, J. Nelson, *J. Am. Chem. Soc.* **2012**, *134*, 685.
[60] W. Zhang, M. Saliba, D. T. Moore, S. K. Pathak, M. T. Hörantner, T. Stergiopoulos, S. D. Stranks, G. E. Eperon, J. A. Alexander-Webber, A. Abate, A. Sadhanala, S. Yao, Y. Chen, R. H. Friend, L. A. Estroff, U. Wiesner, H. J. Snaith, *Nat. Commun.* **2015**, *6*, 6142.
[61] D.-Y. Son, J.-W. Lee, Y. J. Choi, I.-H. Jang, S. Lee, P. J. Yoo, H. Shin, N. Ahn, M. Choi, D. Kim, N.-G. Park, *Nat. Energy* **2016**, *1*, 16081.
[62] P. Fassl, V. Lami, A. Bausch, Z. Wang, M. T. Klug, H. J. Snaith, Y. Vaynzof, *Energy Environ. Sci.* **2018**, *11*, 3380.
[63] H. Tsai, R. Asadpour, J.-C. Blancon, C. C. Stoumpos, O. Durand, J. W. Strzalka, B. Chen, R. Verduzco, P. M. Ajayan, S. Tretiak, *Science* **2018**, *360*, 67.
[64] M. De Bastiani, G. Dell'Erba, M. Gandini, V. D'Innocenzo, S. Neutzner, A. R. S. Kandada, G. Grancini, M. Binda, M. Prato, J. M. Ball, *Adv. Energy Mater.* **2016**, *6*, 1501453.
[65] D. W. DeQuilettes, W. Zhang, V. M. Burlakov, D. J. Graham, T. Leijtens, A. Osherov, V. Bulović, H. J. Snaith, D. S. Ginger, S. D. Stranks, *Nat. Commun.* **2016**, *7*, 11683.
[66] E. Mosconi, D. Meggiolaro, H. J. Snaith, S. D. Stranks, F. De Angelis, *Energy Environ. Sci.* **2016**, *9*, 3180.
[67] P. P. Khlyabich, B. Burkhart, B. C. Thompson, *J. Am. Chem. Soc.* **2011**, *133*, 14534.
[68] R. A. Street, D. Davies, P. P. Khlyabich, B. Burkhart, B. C. Thompson, *J. Am. Chem. Soc.* **2013**, *135*, 986.
[69] D. Baran, R. S. Ashraf, D. A. Hanifi, M. Abdelsamie, N. Gasparini, J. A. Röhr, S. Holliday, A. Wadsworth, S. Lockett, M. Neophytou, C. J. M. Emmott, J. Nelson, C. J. Brabec, A. Amassian, A. Salleo, T. Kirchartz, J. R. Durrant, I. McCulloch, *Nat. Mater.* **2017**, *16*, 363.
[70] J.-F. Guillemoles, T. Kirchartz, D. Cahen, U. Rau, *Nat. Photonics* **2019**, *13*, 501.
[71] J. J. Yoo, S. Wieghold, M. C. Sponseller, M. R. Chua, S. N. Bertram, N. T. P. Hartono, J. S. Tresback, E. C. Hansen, J.-P. Correa-Baena, V. Bulović, *Energy Environ. Sci.* **2019**, *12*, 2192.
[72] S. Gharibzadeh, B. Abdollahi Nejand, M. Jakoby, T. Abzieher, D. Hauschild, S. Moghadamzadeh, J. A. Schwenzer, P. Brenner, R. Schmager, A. A. Haghighirad, *Adv. Energy Mater.* **2019**, *9*, 1803699.
[73] S. Wang, T. Sakurai, W. Wen, Y. Qi, *Adv. Mater. Interfaces* **2018**, *5*, 1800260.
[74] P. Schulz, D. Cahen, A. Kahn, *Chem. Rev.* **2019**, *119*, 3349.
[75] C. M. Wolff, P. Caprioglio, M. Stolterfoht, D. Neher, *Adv. Mater.* **2019**, *31*, 1902762.
[76] J. Haddad, B. Krogmeier, B. Klingebiel, L. Krückemeier, S. Melhem, Z. Liu, J. Hüpkes, S. Mathur, T. Kirchartz, *Adv. Mater. Interfaces* **2020**, *7*, 2000366.
[77] D. Kiermasch, A. Baumann, M. Fischer, V. Dyakonov, K. Tvingstedt, *Energy Environ. Sci.* **2018**, *11*, 629.
[78] T. Kirchartz, J. A. Márquez, M. Stolterfoht, T. Unold, *Adv. Energy Mater.* **2020**, *10*, 1904134.
[79] B. Krogmeier, F. Staub, D. Grabowski, U. Rau, T. Kirchartz, *Sustainable Energy Fuels* **2018**, *2*, 1027.
[80] L. Krückemeier, B. Krogmeier, Z. Liu, U. Rau, T. Kirchartz, *Adv. Energy Mater.* **2021**, https://doi.org/10.1002/aenm.202003489.
[81] K. Akaike, K. Kanai, H. Yoshida, J. y. Tsutsumi, T. Nishi, N. Sato, Y. Ouchi, K. Seki, *J. Appl. Phys.* **2008**, *104*, 023710.
[82] J.-Y. Jeng, K.-C. Chen, T.-Y. Chiang, P.-Y. Lin, T.-D. Tsai, Y.-C. Chang, T.-F. Guo, P. Chen, T.-C. Wen, Y.-J. Hsu, *Adv. Mater.* **2014**, *26*, 4107.
[83] Z.-L. Guan, J. B. Kim, Y.-L. Loo, A. Kahn, *J. Appl. Phys.* **2011**, *110*, 043719.
[84] R. Nakanishi, A. Nogimura, R. Eguchi, K. Kanai, *Org. Electron.* **2014**, *15*, 2912.
[85] P. Caprioglio, C. M. Wolff, O. J. Sandberg, A. Armin, B. Rech, S. Albrecht, D. Neher, M. Stolterfoht, *Adv. Energy Mater.* **2020**, *10*, 2000502.
[86] O. J. Sandberg, J. Kurpiers, M. Stolterfoht, D. Neher, P. Meredith, S. Shoaee, A. Armin, *Adv. Mater. Interfaces* **2020**, *7*, 2000041.
[87] T. C. M. Müller, B. E. Pieters, U. Rau, T. Kirchartz, *J. Appl. Phys.* **2013**, *113*, 134503.
[88] M. Wolf, H. Rauschenbach, *Adv. Energy Convers.* **1963**, *3*, 455.

[89] F. A. Lindholm, J. G. Fossum, E. L. Burgess, *IEEE Trans. Electron Devices* **1979**, *26*, 165.
[90] S. J. Robinson, A. G. Aberle, M. A. Green, *J. Appl. Phys.* **1994**, *76*, 7920.
[91] A. G. Aberle, S. R. Wenham, M. A. Green, presented at *Conf. Record of the Twenty Third IEEE Photovoltaic Specialists Conf. –1993 (Cat. No. 93CH3283-9)*, Louisville, KY, USA, May **1993**.
[92] M. A. Green, *Sol. Cells* **1982**, *7*, 337.
[93] P. Rostan, U. Rau, V. Nguyen, T. Kirchartz, M. Schubert, J. Werner, *Sol. Energy Mater. Sol. Cells* **2006**, *90*, 1345.
[94] N. F. Mott, R. W. Gurney, **1948**.
[95] T. Kirchartz, *Beilstein J. Nanotechnol.* **2013**, *4*, 180.
[96] J. A. Röhr, *Phys. Rev. Appl.* **2019**, *11*, 054079.
[97] J. A. Röhr, T. Kirchartz, J. Nelson, *J. Phys.: Condens. Matter* **2017**, *29*, 205901.
[98] P. Mark, W. Helfrich, *J. Appl. Phys.* **1962**, *33*, 205.